J. Fluid Mech. (2022), *vol*. 939, A14, doi:10.1017/jfm.2022.195

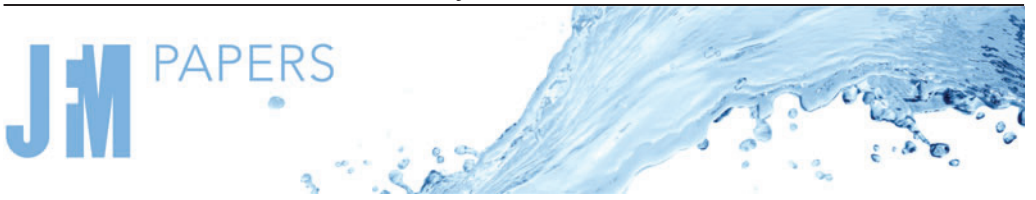

Experimental evidence for the boundary zonal flow in rotating Rayleigh–Bénard convection

Marcel Wedi[1,2], Viswa M. Moturi[1,3], Denis Funfschilling[3] and Stephan Weiss[1,4,5,†]

[1]Max Planck Institute for Dynamics and Self-Organization, Am Fassberg 17, 37077 Göttingen, Germany

[2]Institute for the Dynamics of Complex Systems, Georg-August University, Friedrich-Hund-Platz 1, 37077 Göttingen, Germany

[3]ICube, Université de Strasbourg, 2 Rue Boussingault, 67000 Strasbourg, France

[4]Max Planck – University of Twente Center for Complex Fluid Dynamics

[5]Institute of Aerodynamics and Flow-Technology, German Aerospace Center, Bunsenstr. 10, 3073 Göttingen, Germany

(Received 10 June 2021; revised 25 January 2022; accepted 28 February 2022)

We report on the presence of the *boundary zonal flow* in rotating Rayleigh–Bénard convection evidenced by two-dimensional *particle image velocimetry*. Experiments were conducted in a cylindrical cell of aspect ratio $\Gamma = D/H = 1$ between its diameter (D) and height (H). As the working fluid, we used various mixtures of water and glycerol, leading to Prandtl numbers in the range $6.6 \lesssim Pr \lesssim 76$. The horizontal velocity components were measured at a horizontal cross-section at half height. The Rayleigh numbers were in the range $10^8 \leq Ra \leq 3 \times 10^9$. The effect of rotation is quantified by the Ekman number, which was in the range $1.5 \times 10^{-5} \leq Ek \leq 1.2 \times 10^{-3}$ in our experiment. With our results we show the first direct measurements of the *boundary zonal flow* (BZF) that develops near the sidewall and was discovered recently in numerical simulations as well as in sparse and localized temperature measurements. We analyse the thickness δ_0 of the BZF as well as its maximal velocity as a function of Pr, Ra and Ek, and compare these results with previous results from direct numerical simulations.

Key words: Bénard convection, rotating flows, rotating turbulence

1. Introduction

Rotating thermal convection is a widespread natural phenomenon that also plays a crucial role in various industrial applications. For example, the development of Rossby waves in oceans (Chelton & Schlax 1996) and the flow structures of the atmosphere on Jupiter (Heimpel, Aurnou & Wicht 2005; Reuter *et al.* 2007) are caused by Coriolis forces acting

† Email address for correspondence: stephan.weiss@ds.mpg.de

on fluid motion, which itself is driven by temperature differences between the poles, the equatorial regions and the planet's interior (Zhang & Schubert 1996). In particular, highly turbulent flows involving many different length scales – such as, for example, inside the Sun – are far from being understood and cannot be resolved sufficiently well by state of the art numerical simulations. Thus we rely mostly on simple scaling models that we hope also hold for large-scale systems.

For decades, Rayleigh–Bénard convection (RBC) has been widely used as an idealized model system to investigate convection and its underlying physical phenomena. In this system, a fluid is confined between two horizontal plates at distance H apart from each other, with the lower one at a temperature difference Δ warmer than the upper one. The underlying equations depend only on two dimensionless control parameters, namely

$$Ra = \frac{g\alpha \Delta H^3}{\nu\kappa}, \quad \text{the Rayleigh number,} \tag{1.1}$$

and

$$Pr = \frac{\nu}{\kappa}, \quad \text{the Prandtl number.} \tag{1.2}$$

Here, g denotes the gravitational acceleration, α the isobaric expansion coefficient, ν the kinematic viscosity, and κ the thermal diffusivity. For a laterally extended system, convection sets in above a critical Rayleigh number $Ra_c \approx 1708$ in the form of steady laminar convection rolls, which become unsteady with increasing Ra, and the flow eventually becomes turbulent for very large Ra.

For turbulent convection, one is usually interested in the vertical heat transport, which is expressed by the non-dimensional Nusselt number

$$Nu = \frac{qH}{\lambda \Delta}. \tag{1.3}$$

Here, q is the time averaged heat flux from the bottom to the top plate, and λ is the heat conduction coefficient. Experiments and simulations have been conducted and theoretical models have been proposed to find the correct exponents b and c in the power-law relations $Nu \propto Ra^b\, Pr^c$ (see e.g. Malkus 1954; Grossmann & Lohse 2000, 2002; Ahlers, Grossmann & Lohse 2009; Zhong & Ahlers 2010; He *et al.* 2012). Due to rotational symmetry, most experiments and many numerical investigations have been conducted in upright cylinders, hence the aspect ratio $\Gamma = D/H$ between cylinder diameter $D = 2R$ and height H is a parameter quantifying the geometrical constraints. The height H is a good length scale in RBC only for sufficiently large Γ because only then is Nu independent of Γ (Ahlers *et al.* 2022; Zwirner *et al.* 2021). Nevertheless, most experiments are conducted in cylinders of Γ close to 1 in order to maximize H, and in this way Ra. In such cases, the turbulent flow organizes itself in a large-scale circulation (LSC), which, depending on the aspect ratio, spans the entire domain (Krishnamurti & Howard 1981; Sano, Wu & Libchaber 1989; Ciliberto, Cioni & Laroche 1996) so that warm fluid rises along one side and cold fluid sinks on the opposite side.

Rotation is usually assumed to be around the vertical axis with rotation rate Ω. This leads to additional dimensionless control parameters. When the buoyancy should be compared to the Coriolis forces, one usually considers the *Rossby number*

$$Ro = \frac{\sqrt{g\alpha \Delta / H}}{2\Omega}. \tag{1.4}$$

If one is, rather, interested in the ratio between viscous and Coriolis forces, then the *Ekman number* (*Ek*) is more appropriate. These numbers are related by

$$Ek = \frac{\nu}{H^2\Omega} = 2Ro\sqrt{\frac{Pr}{Ra}}. \tag{1.5}$$

We note that the definition of *Ek* sometimes differs by a factor of two in the literature. The influence of rotation on the flow field and the heat transport is non-trivial because multiple different mechanisms become important, hence making it complicated to deduce simple scaling laws of the form $Nu \propto Ek^a\, Ra^b\, Pr^c$. Finding such scaling laws, however, is vital for understanding rotating turbulent convection, in particular in geophysical and astrophysical systems with *Ra* and *Ek* being out of reach for lab experiments or numerical simulations.

When rotation is applied to a fully turbulent RBC flow, multiple different regimes have been observed as a function of the rotation rate. For low rotation rates, i.e. small $1/Ro$, Coriolis forces barely affect the flow, and the LSC still exists and transports the majority of the heat. This regime is referred to as the *rotation-unaffected regime*.

With increasing rotation rate, the LSC breaks down and is replaced by vortices that start to form from rising (sinking) warm (cold) plumes emerging from the bottom (top) boundary layer. Within these vortices, Ekman pumping occurs, where warm (cold) fluid is efficiently pumped across the thermal boundary layer, leading to an enhancement in the global heat transport for fluids with $Pr > 1$, which sets in with a rather sharp transition at $1/Ro_c$ (see e.g. Rossby 1969; Zhong, Ecke & Steinberg 1993; Julien *et al.* 1996; Liu & Ecke 1997; Kunnen, Clercx & Geurts 2006; Weiss & Ahlers 2011*a*). This enhancement is absent for $Pr < 1$ (Rossby 1969; Zhong *et al.* 2009; Horn & Shishkina 2015; Weiss, Wei & Ahlers 2016; Wedi *et al.* 2021). The regime is often called the rotation-affected regime (see e.g. Kunnen 2020). We note that the global heat transport within this regime exhibits, under certain conditions, rather sharp changes (see e.g. Wei, Weiss & Ahlers 2015), suggesting that there the interplay of multiple different mechanisms leads to various sub-regimes with different functional relations between *Nu*, *Ro* and *Ra*.

With increasing $1/Ro$, the vortices extend and eventually form vertical columns spanning the entire cell (Stellmach *et al.* 2014; Plumley *et al.* 2016). In this so-called *rotation-dominated regime*, the global heat transport decreases with increasing rotation rates due to the *Taylor–Proudman* (Taylor 1921; Proudman 1916) theorem, which states that vertical gradients and therefore also the vertical velocity, are suppressed by Coriolis forces. Hence for sufficiently fast rotation, convection is suppressed entirely. Then buoyancy is too weak to overcome the damping Coriolis forces, and *Ra* needs to be raised above a threshold value Ra_c for convection to occur. For a laterally infinite system, this critical Rayleigh number is $Ra_c \approx 3(\pi^2/2)^{2/3}Ek^{-4/3}$ (Chandrasekhar 1961), independent of *Pr*.

However, in laterally confined cylinders, convection occurs close to the sidewall already for smaller *Ra*, namely above $Ra_w \approx \pi^2(6\sqrt{3})^{1/2}Ek^{-1}$. The flow then takes the form of azimuthal *wall modes* (see e.g. Rossby 1969; Buell & Catton 1983; Zhong, Ecke & Steinberg 1991; Ecke, Zhong & Knobloch 1992; Goldstein *et al.* 1993; Herrmann & Busse 1993; Kuo & Cross 1993; Zhong *et al.* 1993; Zhang & Liao 2009; Favier & Knobloch 2020). While the influence of these wall modes on the heat transport and the flow field is significant close to Ra_w, it was expected that the sidewall influence is negligible for larger *Ra*, when the flow is turbulent. Then the relevant horizontal length scales are small and the sidewall was thought to effect the flow in its direct vicinity only via a thin viscous boundary layer. This assumption has been shown to be false with the recent discovery

of the *boundary zonal flow* (BZF), a new flow state that occurs in rotating RBC (de Wit *et al.* 2020; Zhang *et al.* 2020). The BZF occurs close to the lateral sidewall and plays an important role for the global heat transport in confined systems (see § 2). Although sparse pointwise temperature measurements (Wedi *et al.* 2021) agree with simulations (Shishkina 2020; de Wit *et al.* 2020; Zhang *et al.* 2020), the BZF has so far not been observed directly experimentally. The goal of this paper is to close this gap. Thanks to particle image velocimetry (PIV) measurements of the azimuthal velocity along a horizontal cross-section at mid-height, the thickness and maximum velocity of the BZF could be measured and analysed.

The paper is organized as follows. In the next section we will explain some properties of the BZF in more detail, and we will also reinterpret previous experimental measurements in light of this newly found flow structure. Then, in § 3, we explain the experimental set-up, followed by a section about the measurement results (§ 4). The paper finishes with a conclusion (§ 5).

2. The boundary zonal flow

The BZF is observed as a region close to the sidewall, with a positive time-averaged azimuthal velocity $\langle u_\phi \rangle$ (cyclonic motion), and a central region of negative azimuthal velocity (anticyclonic motion). In the same region, there is also a strong vertical flow that transports warm fluid from the bottom to the top, and cold fluid towards the bottom. The warm (up) and cold (down) regions are periodic in azimuthal direction, with wavenumber $k = 1$ for aspect ratios $\Gamma = 1/5$ (de Wit *et al.* 2020) and $\Gamma = 1/2$ (Zhang *et al.* 2020), whereas $k = 2\Gamma$ was observed for $\Gamma = 1$ and $\Gamma = 2$ cylinders (Shishkina 2020; Zhang, Ecke & Shishkina 2021*a*). This periodic temperature structure drifts in the retrograde direction and can be detected by temperature probes inside the cylinder sidewall (Wedi *et al.* 2021). Although similar, whether the BZF is a remnant of the wall modes above onset is still unclear. A recent study by Favier & Knobloch (2020) suggests that the BZF's origin is in a nonlinear evolution of the wall modes with increasing Ra.

Even though the BZF has just recently been discovered in numerical simulations, some of its features can be seen in older measurements. We show in figure 1 data from Weiss & Ahlers (2011*b*) and Zhong & Ahlers (2010), taken in rotating cylinders with $\Gamma = 0.5$ (figures 1*a*,*c*) and $\Gamma = 1$ (figures 1*b*,*d*), filled with water ($Pr = 4.38$) as the working fluid. For a better orientation, we mark with vertical black lines the critical inverse Rossby number ($1/Ro_c$) for the onset of heat transport enhancement due to rotation at a constant Ra. One can roughly state that $1/Ro_c$ is the rotation rate at which rotation starts to influence the flow and the heat transport, but where buoyancy is still significantly stronger than Coriolis forces, i.e. the rotation-affected regime.

Figures 1(*a*,*b*) show the energies in the first four azimuthal Fourier modes of the temperature signal in the sidewall at mid-height, calculated based on temperature measurements of 8 thermistors. The first mode represents a state where warm fluid rises along one side and cold fluid sinks at the opposite side. The second mode represents a state with two zones where warm fluid rises (on opposite sides), separated by two zones where cold fluid sinks towards the bottom plate. Let us first have look at figure 1(*b*), which shows data from measurements in $\Gamma = 1$ cylinders. When it was first published, the plot was interpreted as showing that for small rotation rates ($1/Ro < 1/Ro_c$), the LSC consists of a single convection role with warm upflow along one side and cold downflow along the other. As a result, the first Fourier mode is significantly stronger than the others. However, at around $1/Ro_c$, the energy in the first Fourier mode decreases

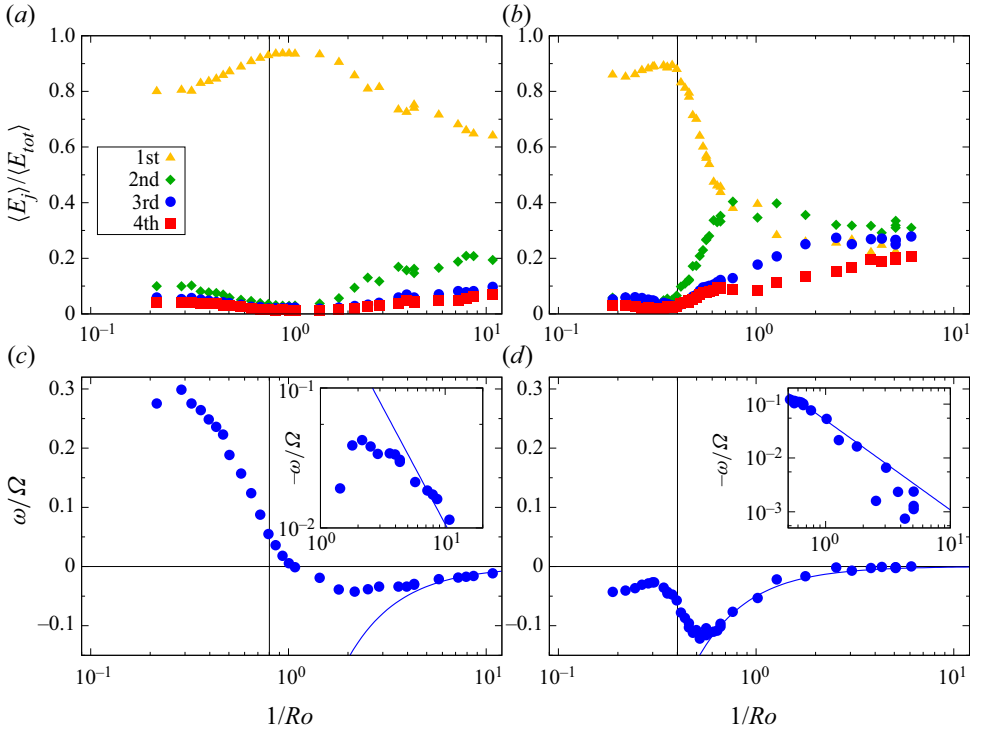

Figure 1. (*a*,*b*) Relative energy in the first four Fourier modes of the azimuthal temperature signal at mid-height of the cell. (*c*,*d*) Relative azimuthal drift of the temperature structure at mid-height normalized by the rotation rate of the convection cell. The solid blue lines in (*c*,*d*) mark power laws $\propto (1/Ro)^{-5/3}$ as suggested by Zhang, Ecke & Shishkina (2021*b*). The insets in (*c*,*d*) show only a subsection of the same data (large $1/Ro$), but multiplied by (-1) and on a log-log plot. (*a*,*c*) Data from experiments with cylindrical $\Gamma = 0.5$ containers ($Ra = 1.8 \times 10^{10}$, $Pr = 4.38$). (*b*,*d*) Data from experiments with cylindrical $\Gamma = 1$ containers ($Ra = 2.25 \times 10^{9}$, $Pr = 4.38$). The vertical solid lines mark the onset of heat transport enhancement at $1/Ro_c = 0.8$ (*a*,*c*) and $1/Ro_c = 0.4$ (*b*,*d*). Plots adapted from figures 4 and 13 of Weiss & Ahlers (2011*b*), and figure 19 of Zhong & Ahlers (2010).

drastically with increasing rotation rates, which is interpreted as the disappearance of the LSC. This decrease of E_1/E_{tot} is accompanied with an increase in particular of the second harmonic. While it was not clear at the time, we now believe that this increase of the second harmonic shows the occurrence of the BZF, which in $\Gamma = 1$ cylinders consists of two warm upflow regions separated by two regions where cold fluid sinks near the sidewall.

Similarly, we interpret the data in figure 1(*a*). The LSC starts to disappear at around $1/Ro_c$, however the energy of the first Fourier mode is still large even beyond $1/Ro_c$ since now the BZF appears, which for $\Gamma = 0.5$ has a wave number $k = 1$. Note that in both cases ($\Gamma = 1/2$ and $\Gamma = 1$), the Fourier energy in the BZF mode decreases with increasing rotation rate. This means not that the BZF disappears, but rather that the temperature difference between warm and cold areas decreases, which to some extent is caused by the finite heat conductivity of the sidewall and a subsequent heat loss. Note that in these experiments, temperatures were measured inside the sidewall with probes not in direct contact with the fluid.

Figure 1(*c*) shows the azimuthal drift rate of the LSC (for small $1/Ro$) or the BZF (for larger $1/Ro$), normalized by the rotation rate of the convection cylinder as a function of $1/Ro$. For $\Gamma = 0.5$ (figure 1*c*), the change of direction from positive (prograde) to negative (retrograde as observed for the BZF) above $1/Ro_c$ is visible. For $\Gamma = 1$ (figure 1*d*), the drift rate is always negative but nevertheless shows a monotonic behaviour similar to that for $\Gamma = 0.5$, in particular beyond $1/Ro_c$. For sufficiently large $1/Ro$, the drift rate increases asymptotically to zero. The solid blue line in figures 1(*c*,*d*) is a power law $\propto (1/Ro)^{5/3}$ as suggested by Zhang *et al.* (2021*b*) based on numerical observation. We see that data for $\Gamma = 0.5$ (figure 1*c*) start to follow this power law only at the largest $1/Ro$, while for $\Gamma = 1$ (figure 1*d*), data follow this power law rather well for $1/Ro > 0.6$ or so. We also remind the reader that in temperature measurements at small Pr, i.e. where no heat transport enhancement is observed, the onset of the BFZ can be determined from the temperature distribution close to the sidewall, which changes from a unimodal (no BZF) to a bimodal distribution (BZF exists) close to $1/Ro = 1$, i.e. just when Coriolis forces start to influence the turbulent flow (Zhang *et al.* 2020; Wedi *et al.* 2021).

The above observations constitute evidence that the BZF starts to form (at least for moderate and larger Pr) already above $1/Ro_c$ in the rotation-affected regime. However, it is unclear at which rotation rates the BZF is fully developed such that its properties (width, strength, drift rate) follow strict power laws in Ek, Ra and Pr over large parameter ranges. Looking at figures 1(*c*,*d*), one can see that a maximal negative drift is reached at $\approx 2/Ro_c$ ($1.5/Ro_c$ for $\Gamma = 1$), above which the (negative) drift rate decreases monotonically with $1/Ro$, suggesting that only then is the BZF fully developed.

It is unclear at this point whether scaling relations of characteristic BZF properties – such as its width or the maximal azimuthal velocity – and the dimensionless control parameters are affected by changes in the bulk flow morphologies (turbulence, plumes, columns, cells). In this context, we also want to point out that even at moderate rotation rates, in the rotation-affected regime, multiple different smaller regimes exist, which were observed in heat flux measurements at large Ra (Wei *et al.* 2015; Weiss *et al.* 2016), and which are unexplained to date. One might speculate that these regimes occur from an interplay of heat transport enhancement due to Ekman pumping, heat transport reduction due to the suppression of vertical velocity (Taylor–Proudman), and additional pumping of heat within the BZF. Understanding the BZF hence also helps us to better understand the seemingly sharp changes in the slope of $\partial Nu/\partial Ro$ for small rotation rates. In this context, it is also important to quantify how much of the heat transport enhancement is due to the Ekman pumping within vortices in the radial bulk, and how much stems from the BZF.

Some features of the BZF, such as the positive azimuthal velocity close to the sidewall, have been observed before (Kunnen *et al.* 2011) and were attributed to Stewartson layers in which fluid is pumped from the Ekman layers at the bottom and the top towards the mid-height of the cell. This explanation is, however, incompatible with the observation of the BZF, in particular since Stewartson layers form when fluid is pumped from the vertical boundaries towards the vertical cell centre. This is in contrast to the long vertical structures observed for the BZF, in which fluid is pumped from the bottom to the top, and vice versa. Furthermore, the Stewartson mechanism assumes a flow towards the sidewalls that is independent of the azimuthal orientation and is not in accordance with the azimuthally periodic, vertical flow structures of the BZF. In addition, simulations at rather small Ek suggest that the thickness of the BZF (δ_0) varies with Ek and Ra as $\delta_0 \sim Ek^{2/3}$ (Zhang *et al.* 2020), which is not compatible with the known Stewartson layer scalings $\delta_s \sim Ek^{1/3}$ and $\delta_s \sim Ek^{1/4}$ (Stewartson 1957, 1966; Kunnen *et al.* 2011) that form

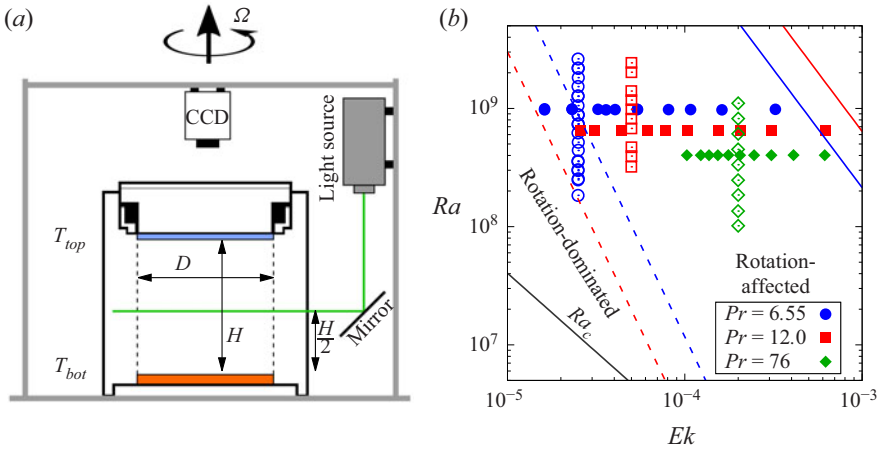

Figure 2. (*a*) Schematic of the experimental set-up. The copper bottom plate is shown in orange; the sapphire top plate is shown in blue. (*b*) Investigated parameter space in an *Ra*–*Ek* plot. Different colours of the symbols show different *Pr* (see legend). Closed symbols mark measurements taken at $Ra = \text{const.}$ (datasets R1, R2, R3), while open symbols mark measurements at $Ek = \text{const.}$ (datasets E1, E2, E3). The black solid line marks the onset of bulk convection according to Chandrasekhar (1961). The solid red and blue lines mark *Ra* below which Coriolis forces affect the flow for the two smallest *Pr*. These lines are calculated based on $1/Ro_c$ for onset of heat transport enhancement reported by Weiss *et al.* (2016). Dashed lines mark *Ra* below which Coriolis forces become dominant over buoyancy and are estimated from the $1/Ro_{max}$ where heat transport is maximal (Weiss *et al.* 2016).

due to Ekman pumping. While in measurements presented in this paper, taken in the rotation-affected (buoyancy-dominated) regime, we find a lower exponent for the thickness close to $\delta_0 \sim Ek^{1/2}$, this is still significantly larger than what is expected for Stewartson layers.

3. Set-up

Our experimental set-up (figure 2*a*) consists of a cylindrical cell with height equal to the diameter 196 mm resulting in an aspect ratio of $\Gamma = 1$. The cell is cut out of a block of acrylic glass and is thus transparent from all sides. A 15 mm thick copper plate with heat conductivity 394 W m $^{-1}$ K^{-1} serves as the bottom plate. It is heated via an electrical wire that is embedded in grooves at its bottom. Neighbouring grooves are 6 mm apart to enable uniform heating. Two thermistors are installed into the plate approximately 3 mm below the fluid interface. As a top plate of the convection cell, we use a 5 mm thick high-conductive sapphire plate, which is cooled by a temperature-controlled water bath. The water temperature is measured with a single thermistor and kept at a desired temperature to within ± 0.02 K via a computer-controlled feedback loop.

The cooling water bath on top of the top plate consists of PVC sides and has a transparent top cover of acrylic glass. This transparent set-up allows optical access from the top for particle image velocimetry (PIV). For this, a Dantec RayPower 2000 laser with cylindrical lens optics is attached inside the rotating structure of the set-up as shown in figure 2(*a*). To measure a horizontal cross-section of the cell, the light sheet is redirected using a mirror from the side and in this way illuminates a horizontal cross-section of the cell at mid-height ($z = H/2$). A high-speed camera (Phantom VEO4K 590-L) is mounted inside the rotating frame above the cell. For illumination, the fluid is seeded with silver-coated

Dataset	T_m (°C)	Pr	Ra	Ek
R1	22.5	6.55	9.8×10^8	1.6×10^{-5}–3.2×10^{-4}
R2	22.5	12.0	6.5×10^8	2.6×10^{-5}–6.2×10^{-4}
R3	22.5	76	4.0×10^8	1.0×10^{-4}–1.2×10^{-3}
E1	22.5	6.55	1.8×10^8–1.8×10^9	2.5×10^{-5}
E2	22.5	12.0	3.2×10^8–2.4×10^9	5.0×10^{-5}
E3	22.5	76	1.0×10^8–1.1×10^9	2.0×10^{-4}
P1	20.0–30.0	5.4–83.3	5.8×10^8	1.0×10^{-4}
P2	20.0–30.0	9.8–83.3	5.9×10^8	5.1×10^{-5}–1.5×10^{-4}

Table 1. Overview of the conducted experiments.

hollow glass spheres of diameter 10 μm. Two-dimensional velocity fields were calculated from the cross-correlation of two consecutive camera snapshots, taken 20 ms apart in most cases, but this value was adapted depending on the free-fall time τ_{ff}. Images were taken until the RAM of the camera (72 GB) was filled, which in all cases ensured a minimum recording time of 100 τ_{ff} (typically about 10 min). The PIV algorithm was performed with ParaPIV within MATLAB (Wang 2018). The resulting velocity field had a resolution of 240×240 velocity points.

The entire set-up was mounted on a rotating table with a frame built on top of it and driven by a Nanotec PD4-C stepper motor. All necessary electrical connections from the lab into the rotating frame were achieved via sliprings at the top and bottom of the rotating frame. At the top, water feed-throughs were installed to supply water to the cooling water bath. The stainless steel feed-throughs were connected with bolts to the rotating frame on one side and to a non-rotating aluminum framework on the other in such a way that it kept the rotating axis fixed in space in order to avoid any precession of the set-up.

As working fluid we used mixtures of deionized water with glycerol. For most experiments, we kept the temperature constant at $T_m = (T_{bot} + T_{top})/2 = 22.5\,^\circ$C, i.e. close to room temperature, in order to minimize heat flux to or from the sides. Different Pr were achieved by using different mass concentrations of glycerol in water, which however also changes the accessible Ra and Ek ranges for a given Pr. In this paper, we focus mostly on the three cases $Pr = 6.55$ (pure water), $Pr = 12.0$ (20 % glycerol) and $Pr \approx 76$ (60 % glycerol). By changing the temperature difference Δ and the rotation rate Ω, we control Ra and Ek. Figure 2(*b*) and table 1 show an overview of the performed experiments. For each Pr, we performed measurement at fixed Ek and various Ra (E1, E2, E3) as well as measurements with one fixed Ra and varying Ek (R1, R2, R3). Due to experimental constraints, different combinations of Ek and Ra were chosen for different Pr. For two experimental runs, P1 and P2, we explored the Pr dependency of the BZF, and there we also changed T_m to easily adjust Pr.

In all measurements, we are far away from the onset of convection ($Ra \gg Ra_c$), as shown in figure 2(*b*). Hence the observed structures close to the walls are results of strongly nonlinear interactions, in contrast to the linear wall modes close to $1/Ro_w$. We also note that most of our measurements are not conducted in the geostrophic regime. Although it is not clear at which Ek the geostrophic regime starts, we can compare our data with heat flux measurements presented in Weiss *et al.* (2016). There, the onset of heat transport enhancement was found to scale like $1/Ro_{c1} \approx 0.75 Pr^{-0.41}$, and it presents a critical rotation rate above which Coriolis forces have a significant influence on the flow. These functions are shown as solid lines in figure 2(*b*). We see that all our

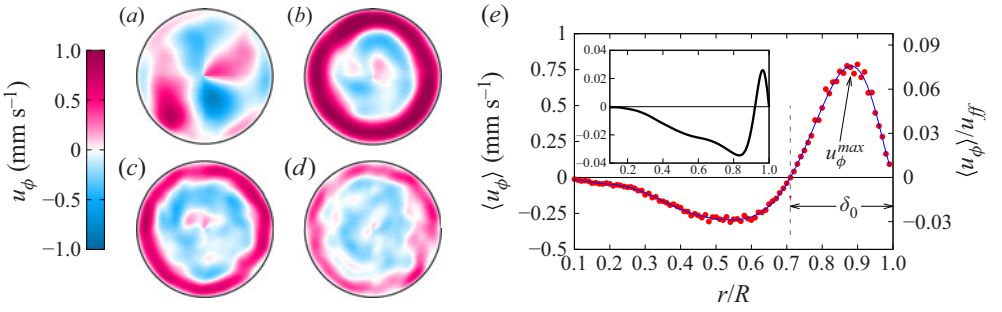

Figure 3. (*a–d*) Time-averaged u_ϕ measured at mid-height for $Ra = 4 \times 10^8$ and $Pr \approx 76$, and $Ek = \infty$ (*a*), $Ek = 6.2 \times 10^{-4}$ (*b*), $Ek = 1.5 \times 10^{-4}$ (*c*), and $Ek = 1.0 \times 10^{-4}$ (*d*). (*e*) Red circles show the azimuthal average of (*c*), in physical units (left-hand *y*-axis) and normalized by the free-fall time (right-hand *y*-axis). The blue solid line is a fit of a polynomial of 10th order. The dashed vertical line marks the BZF thickness δ_0, at which $\langle u_\phi \rangle$ crosses 0; the arrow points to the maximum velocity u_ϕ^{max} within the BZF. The inset shows results from direct numerical simulations (DNS) of the azimuthal velocity normalized by the free-fall velocity, $\langle u_\phi \rangle / u_{ff}$, for $Ra = 10^8$, $1/Ro = 10$, $Pr = 0.8$.

measurements are in this regime. However, we also show as dashed lines the rotation rates $1/Ro_{max} \approx 21.4\, Pr^{1.37}\, Ra^{-0.18}$, at which the heat transport was maximal (Weiss *et al.* 2016). Only for larger rotation rates did the Coriolis forces cause a clear suppression of the heat flux. We therefore believe that the geostrophic regime must be to the left of the dashed lines. We see that our data are in the rotation-affected regime but not in the rotation-dominated regime.

4. Results

4.1. *Radial velocity profile*

The horizontal velocity in Cartesian coordinates (u, v) is first transformed into polar coordinates $u_r = u\cos(\phi) + v\sin(\phi)$ and $u_\phi = -u\sin(\phi) + v\cos(\phi)$. Here, r is the radial distance from the cell centre, and ϕ is the polar angle. We show in figures 3(*a–d*) time-averaged azimuthal velocity fields $\langle u_\phi(r, \phi) \rangle_t$ for different Ek.

One can see how the structure of the flow changes qualitatively. In the non-rotating case ($Ek = \infty$), the flow field does not show a clear difference between the radial centre and the regions close to the sidewall. Instead, the distribution of the red ($\langle u_\phi \rangle_t > 0$) and blue ($\langle u_\phi \rangle_t < 0$) is orderless. In fact one would expect in this case that due to the turbulent motion, the time-averaged azimuthal velocity would be very small. This is, however, not the case, since there is a rather persistent large-scale motion, i.e. the LSC, that is steady over the time duration of our measurement. Under rotation (figures 3*b–d*), the characteristic features of the BZF become clearly visible, namely a red ring ($\langle u_\phi \rangle_t > 0$) surrounding a blue central region ($\langle u_\phi \rangle_t < 0$). It can be observed that with increasing rotation rates, the width of the red cyclonic zone decreases as well as the strength of the flow.

For a more quantitative analysis, we average the velocity in the azimuthal direction. For this, we sum over all velocity vectors at radial distances between r and $r + \mathrm{d}r$ away from the centre, and divide this sum by the number of voxels in this range (N_r):

$$\langle u_\phi \rangle(r) = \frac{1}{N_r} \sum_{r}^{r+\mathrm{d}r} \langle u_\phi \rangle_t. \tag{4.1}$$

As an example, we show in figure 3(*e*) $\langle u_\phi \rangle$ calculated from the field in figure 3(*c*). The red points show the calculated velocities. The blue line is a polynomial fit of degree 10 to these points that allows quantitative analysis. We also show for comparison, in the inset of figure 3(*e*), results from simulations at very similar *Ra* and *Ro* but smaller $Pr = 0.8$ (Zhang *et al.* 2021*a*). At first glance, our radial profile of $\langle u_\phi \rangle$ looks very similar qualitatively to the results from direct numerical simulations (DNS). But on a closer look, quantitative differences become visible. The most obvious is the width of the BZF, i.e. the distance δ_0 from the wall, where $\langle u_\phi \rangle$ switches sign, is much smaller in the DNS than in our case. This discrepancy is most likely due to the difference in *Ek* (1.8×10^{-5} compared to 1.5×10^{-4} for our measurement). While DNS were conducted within the rotation-dominated regime, our measurements were acquired in the rotation-affected regime. Even though *Pr* is different between DNS and our simulation by a factor of 10, from Zhang *et al.* (2021*a*) we expect no, or only a very small *Pr* dependency of δ_0 in the investigated *Pr* range.

In the following, we will analyse some features of the radial profile as functions of the dimensionless control parameters. One of these features is the radial position r_0, where $\langle u_\phi \rangle$ switches sign, i.e. where the BZF and the bulk flow separate. To be in agreement with previous publications (Zhang *et al.* 2020, 2021*a*), we define the width of the BZF as $\delta_0 = (R - r_0)/R$.

Figure 4 shows various time- and azimuthally-averaged velocity profiles for different control parameters. To compare with DNS, the velocity profiles are normalized by the free-fall velocity $u_{ff} = \sqrt{\alpha g H \Delta}$. In figures 4(*a*,*c*), *Ra* was kept constant and *Ek* was changed. The azimuthal velocity amplitude inside the BZF decreases with increasing rotation rate (decreasing *Ek*). This decrease with decreasing *Ek* is by no means obvious. On one hand, we know that increasing rotation suppresses fluid motion, hence a reduced velocity is expected. While this is certainly true for sufficiently fast rotation rates, for moderate rotation rates and *Pr* discussed here, the heat flux (*Nu*) is enhanced, which suggests at least a faster flow in the z-direction. Also note that the rate with which potential energy is converted into kinetic energy, and finally dissipated into heat, is proportional to *Nu* i.e. $\varepsilon_u = (\nu^3/H^4)(Nu - 1)\, Ra\, Pr^{-2}$. Therefore, the total kinetic energy in the fluid is expected to increase with increasing rotation rates first.

The fact that we nevertheless see a decrease here for all rotation rates might be because the additional kinetic energy is contributing mostly to vertical velocity. In addition, the width of the BZF becomes smaller, hence also viscous drag would lead to a further reduction of the maximal azimuthal velocity inside the BZF.

In figures 4(*b*,*d*), *Ek* is kept constant and plots are shown for different *Ra*. The maximal velocities increase with increasing *Ra*, which can be explained with the enhanced thermal driving. However, we want to remind the reader that here, we show the azimuthal velocity normalized by the free-fall velocity $u_{ff} = \sqrt{g\alpha \Delta H} = Ra^{1/2}(\nu\kappa)^{1/2}/H$. In fact, the Reynolds number $Re = UH/\nu$, and hence also the typical velocity scale U in non-rotating RBC, scales as $Re \sim Ra^\zeta$, with ζ determined experimentally to be in the range $\zeta \approx 0.42 \ldots 0.5$ (see e.g. Sun & Xia 2005; Brown, Funfschilling & Ahlers 2007), which would lead to $U/u_{ff} \propto Ra^{-0.08 \ldots 0}$, i.e. a decrease with increasing *Ra*. Hence the azimuthal velocity in the BZF increases significantly faster with *Ra* than for non-rotating RBC.

In the following, we will analyse these profiles quantitatively. Most importantly, we look at the width δ_0, as well as the maximal velocity u_ϕ^{max} and its location δ_{max}, as functions of the control parameters *Ek*, *Ra* and *Pr*.

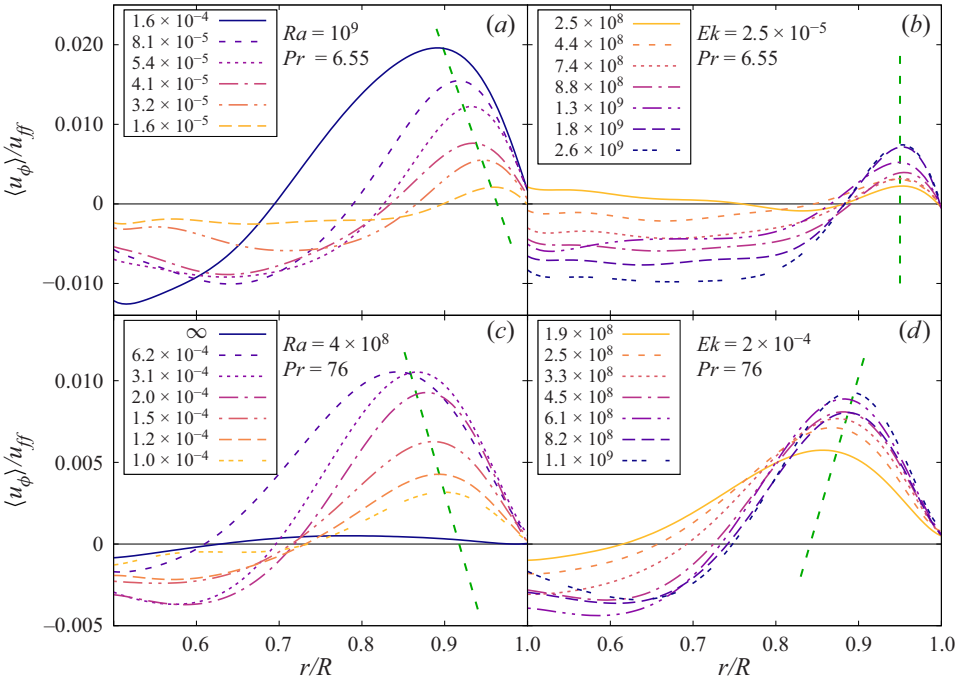

Figure 4. Radial profiles of $\langle u_\phi \rangle$ for $Ra =$ const. and changing Ek (*a*,*c*), and changing Ra at $Ek =$ const. (*b*,*d*), as in the legends. (*a*,*b*) $Pr = 6.55$; (*c*,*d*) $Pr = 76$. Green dashed lines are guides to the eye and connect the velocity maxima inside the BZF measuring $\delta_{u_\phi^{max}}$ (see also figure 7).

4.2. *BZF width* δ_0

We begin by calculating the zero-crossing and hence the thickness δ_0 as functions of the rotation rate. These results are presented in figure 5. In figure 5(*a*), we show δ_0 as a function of $1/Ro$ for three different Ra. Note that here we have chosen to plot $1/Ro$ on the x-axis, because as was shown in previous studies, different features of the heat transport seem to depend predominantly on $1/Ro$ and depend only weakly on Ra, such as the onset of heat transport enhancement in large Pr fluids (Weiss *et al.* 2016) or the decrease of Nu in small Pr fluids (Wedi *et al.* 2021).

We see in figure 5(*a*) that δ_0 decreases with increasing $1/Ro$ for all three datasets. We have seen in figure 2(*b*) that our data are in the rotation-affected regime but not in the rotation-dominated regime, and that we are particularly far from the geostrophic regime for $Pr = 76$. Also considering the trend of the green data points, we decide to set a somehow arbitrary threshold for the rotation rate, which is $1/Ro_t = 1$ for $Pr = 6.55$ and $Pr = 12.0$, and $1/Ro_t = 3$ for $Pr = 76$. In the following, we will mark data points at small and larger $1/Ro \geq 1/Ro_t$ with open and closed symbols, respectively, and will use only the closed symbols for scaling analysis. While this decision is somewhat arbitrary, we will see below that solid symbols often follow certain scaling relations from which the open symbols diverge. Now we fit power laws of the form $\delta_0 \sim (1/Ro)^{-\alpha}$ to the data for which $1/Ro \geq 1/Ro_t$ (solid symbols in figure 5).

The resulting power laws are shown as dashed lines in figure 5(*a*) and have exponents $\alpha_{6.55} = 0.52 \pm 0.03$, $\alpha_{12} = 0.30 \pm 0.02$ and $\alpha_{75} = 0.07 \pm 0.03$, with the subscript being Pr. At first glance, these three different power laws suggest that the exponent α is itself

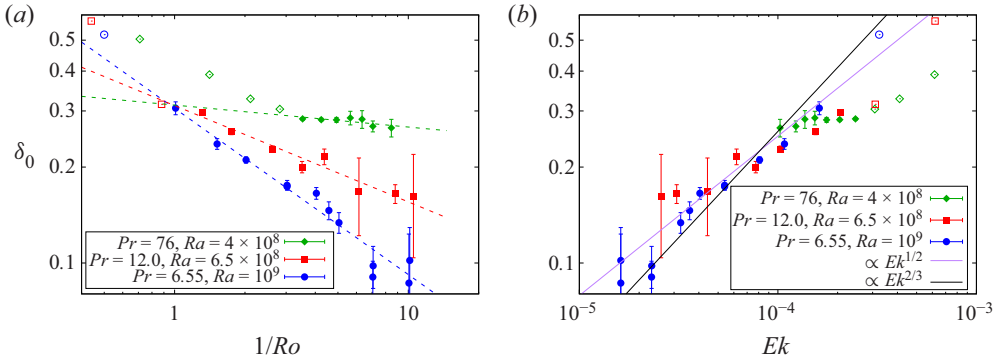

Figure 5. BZF width δ_0 as a function of the rotation rate for datasets E1 (blue circles), E2 (red squares) and E3 (green diamonds). Open symbols mark data with $1/Ro < 1/Ro_c$. Closed symbols mark data with $1/Ro \geq 1/Ro_c$ (see text for further information). The error bars were estimated from the scatter of the data points around the fitted polynomial close to δ_0. Panel (*a*) shows δ_0 as a function of $1/Ro$ on a log-log plot. The dashed lines are power-law fits to the solid symbols ($1/Ro \geq 1/Ro_c$). Panel (*b*) shows the same data plotted against Ek. The black line is a power law $\propto Ek^{2/3}$ as suggested by Zhang *et al.* (2021*a*). The purple line is a power law $\propto Ek^{1/2}$.

dependent on Ra and/or Pr, and that no simple scaling law of the form

$$\delta_0 = A\, Ek^{\alpha}\, Ra^{\beta}\, Pr^{\gamma} = 2^{\alpha} A\, Ro^{\alpha}\, Ra^{\beta-\alpha/2}\, Pr^{\gamma+\alpha/2}, \tag{4.2}$$

can be found, even though such simple scalings have been suggested recently based on numerical simulations (Zhang *et al.* 2021*a*), namely (for $Pr > 1$)

$$\delta_0 \propto \Gamma^0\, Pr^0\, Ra^{1/4}\, Ek^{2/3}. \tag{4.3}$$

For comparison with data from simulations, we plot in figure 5(*b*) the same measured data but now as functions of their respective Ek. Now the data for very different Ra and Pr overlap surprisingly well, for a given Ek. The black solid line in figure 5(*b*) is $\propto Ek^{2/3}$ as found in simulations by Zhang *et al.* (2021*a*), but is ignoring the Ra-dependency. We also show by a purple line a scaling $\propto Ek^{1/2}$ for comparison. Here, our data seem to agree better with the purple line ($\propto Ek^{1/2}$), in particular for larger Ek. However, we also note that the data scatter significantly and have rather large error bars, in particular for small Ek, where the influence of buoyancy is small. Deviations from either power law occur mostly for larger Ek, where also the buoyancy becomes more important. A firm conclusion on which exponent represents the data better cannot be drawn from these data.

Clearly, there is either a simple power-law relation as in (4.2), or something more complicated as figure 5(*a*) suggests. In the case of a simple power-law relation (as in (4.2)), we can at least state from figure 5(*b*) that δ_0 might depend predominantly on Ek, but is otherwise at most very weakly dependent on Ra and Pr, at least in the range of our investigation.

Observations from DNS (see (4.3)) indeed suggest an independence from Pr, but also found an Ra-dependency $\delta_0 \propto Ra^{1/4}$. Let us have a closer look at what our data have to say. Figure 6(*a*) shows δ_0 as function of Ra for three different Pr and different but constant Ek. While the data with $Pr = 76$ (largest Ek) suggest a scaling of the BZF width $\delta_0 \sim Ra^{\beta}$ with $\beta = -0.19 \pm 0.01$, for smaller Pr (and also smaller Ek), δ_0 seems to be unaffected by Ra, i.e. $\beta \approx 0$. As before, the error bars are estimates from the scatter of the velocity data points around the fitted polynomial close to δ_0. Again here, it seems that the exponent

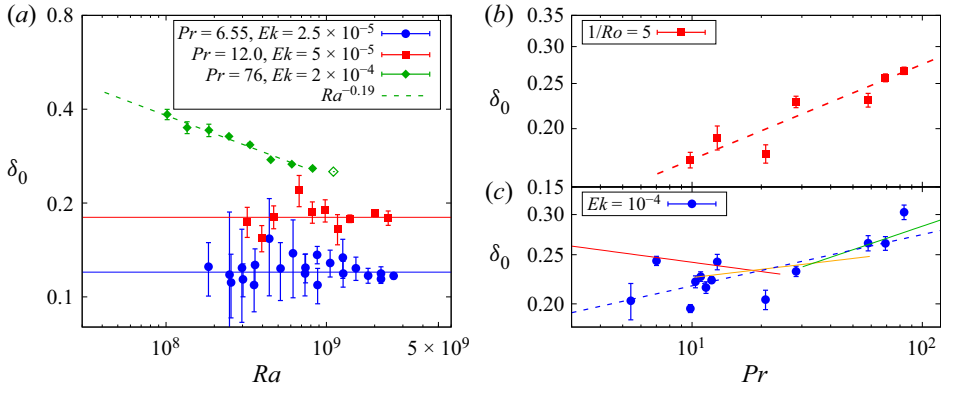

Figure 6. (*a*) Thickness δ_0 as a function of Ra for three different datasets: E1 ($Pr = 6.55$, $Ek = 2.5 \times 10^{-5}$, blue circles), E2 ($Pr = 12.0$, $Ek = 5 \times 10^{-5}$, red squares) and E3 ($Pr = 76$, $Ek = 2 \times 10^{-4}$, green diamonds). The error bars were estimated from the scatter of the data points around the fitted polynomial close to δ_0. The green dashed line is a power law with exponent $\gamma = -0.19 \pm 0.01$. The red and blue horizontal lines are constants with $\delta_0 = 0.18$ and 0.12. (*b*) Thickness δ_0 as a function of Pr for $Ra = 6 \times 10^8$ and $1/Ro = 5$ (dataset P2). The red dashed line is a power-law fit with $\sim Pr^{0.20 \pm 0.05}$. (*c*) Thickness δ_0 as a function of Pr for $Ra = 6 \times 10^8$ and $Ek = 10^{-4}$ (dataset P1). The red, orange and green lines are functions $A_1 Pr^{\gamma}$ with the values listed in table 2. The dashed blue line marks a power law $\propto Pr^{0.1}$.

β is a function of Pr. Note in particular that for $Pr = 76$, δ_0 decreases with increasing Ra, which is in disagreement with the results of DNS.

In figures 6(*b*,*c*), we show δ_0 as a function of Pr for constant Ra. Experimentally, Pr was varied by changing either T_m or the concentration of glycerol in the aqueous working fluid. While it is trivial to set the system to the desired Ra by changing Δ accordingly, the rotation rate Ω needed to be adjusted to keep either Ek or Ro constant. We did both.

Let us first have a look at figure 6(*b*), where $1/Ro = 5$. As can be seen, the data are rather noisy and do not increase strictly monotonically with Pr. There is, however, a clear trend that δ_0 increases with increasing Pr, as suggested by the previous measurements. Fitting a power law of the form $\delta_0 \sim Pr^{\gamma_1}$ to the data yields $\gamma_1 = 0.2 \pm 0.05$.

We show in figure 6(*c*) values of δ_0 that were acquired at constant Ra, constant Ek and varying Pr. The data scatter significantly, and no clear trend is obvious. Here, δ_0 looks rather constant for small Pr, and seems to increase for larger Pr. While the red squares in figure 6(*b*) and the blue circles in figure 6(*c*) show different datasets, the data are related via (4.2). In particular, we see from (4.2) that $\gamma_1 = \gamma + \alpha/2$.

We assume for a moment that δ_0 can be represented by power laws as in (4.2), but that the exponents α, β and γ are different for the three different Pr ranges, as observed in figures 5(*a*) and 6(*a*). We list in table 2 the fitted parameters from figure 5(*a*) as well as figures 6(*a*,*b*). With this, we can calculate the expected power laws $A_1\, Pr^{\gamma}$, with $A_1 = A\, Ek^{\alpha}\, Ra^{\beta}$, for all three Pr ranges, which we show in figure 6(*c*) as solid lines. Due to the different exponents α for different Pr, we also get different exponents γ, which would explain the somewhat non-monotonic behaviour of the data points in figure 6(*c*). Indeed, the lines represent somehow the non-monotonic behaviours of the data points. Of course, assuming a power law with a varying exponent means that there is no real power law in the investigated range. However, this approach shows that the two different datasets are consistent with each other. We note that one could have also fitted a power law through the blue points in figure 6(*c*), resulting in a single exponent $\propto Pr^{0.1 \pm 0.03}$ (blue dashed

Pr	A	α	β	$\beta-\alpha/2$	$\gamma+\alpha/2$	A_1	γ
6.55	34.0	0.522	0	−0.261	0.20	0.278	−0.061
12.0	2.93	0.292	0	−0.146	0.20	0.199	0.054
76	15.23	0.092	−0.19	−0.236	0.20	0.140	0.154

Table 2. Coefficient and power-law exponent estimates from (4.2). The α values were estimated based on the data in figure 5(a). The A and β values are estimates from figure 6(a), and γ was estimated from figure 6(b).

line) over the entire range. One could then represent the data in figure 6(b) with different power laws for different Pr ranges. In any case, we have learned from figure 6(c) that (i) the Pr dependency is rather small when Ek is kept constant, and (ii) the Ra, Pr and Ek dependencies of δ_0 cannot be written by simple power laws in the parameter range that we are investigating here (i.e. the rotation-affected regime).

So far we have analysed δ_0, the width of the BZF, as it can be measured easily in the time-averaged two-dimensional velocity field shown in figures 3(a–d). However, the strength of the flow, represented by the maximal averaged azimuthal velocity u_ϕ^{max}, is another quantity characteristic for the BZF, which can help to reveal the mechanisms leading to this zonal flow. Therefore, we show in figures 7(a,b) the compensated time-averaged maximal velocity $u^*_{max} = u_\phi^{max}\, Ra\, Pr^{0.8}$, and in figures 7($c$,$d$) its location measured as the distance from the sidewall δ_{max}. These data are plotted against $Ra\, Ek$ on the x-axis, as this represents the Rayleigh number compared to its critical value for the onset of wall modes ($Ra_w \propto Ek^{-1}$). We show in figures 7(a,c) data that were acquired at constant Ek for a given Pr and varying Ra, whereas figure 7(b,d) show data with constant Ra and different Ek.

Let us first have a look at the compensated maximal averaged azimuthal velocity u^*_{max} shown in figure 7(a). Note that the definition of u^*_{max} is not based on scaling arguments, but is rather an empirical relation that provides a very good collapse of data onto a single power law for all three Pr, with each having a different Ek. The black solid line marks $u^*_{max} = 4.7(Ek\, Ra)^{3/2}$ (or equivalently $u_\phi^{max} = 4.7\, Ek^{3/2}\, Ra^{1/2}\, Pr^{-0.8}$), which represents the data fairly well. We show the same function as a black line also in figure 7(b), but now compare it with measurements that were acquired at constant Ra but varying Ek. We see that data for small values of $Ek\, Ra$ follow this law, but data for large values of $Ek\, Ra$ diverge from the straight line. For a better visual separation, data with $1/Ro \geq 1/Ro_t$ were plotted with solid symbols, whereas data for which $1/Ro < 1/Ro_t$ were plotted with open symbols. As mentioned previously, we assumed $1/Ro_t = 1$ for the two smaller Pr, and $1/Ro_t = 3$ for $Pr = 76$. Since data for varying Ra follow the mentioned power law for nearly two decades, we are confident that this power law also holds for smaller Ek, at least as long as buoyancy plays a significant role. Whether this scaling holds even in the rotation-dominated regime, however, remains unclear.

Figures 7(c,d) show the distance from the wall to the maximal velocity δ_{max}, normalized by $\sqrt{Ek}$ and plotted against $Ek\, Ra$. Measurements are the same as for figures 7(a,b), which means constant Ek for figure 7(c), and constant Ra for figure 7(d). We see that the data collapse fairly well on a constant $\delta_{max}/\sqrt{Ek} \approx 10$ or so. The inset in figure 7(c) shows that data do not collapse on top of each other without this normalization. However, the green

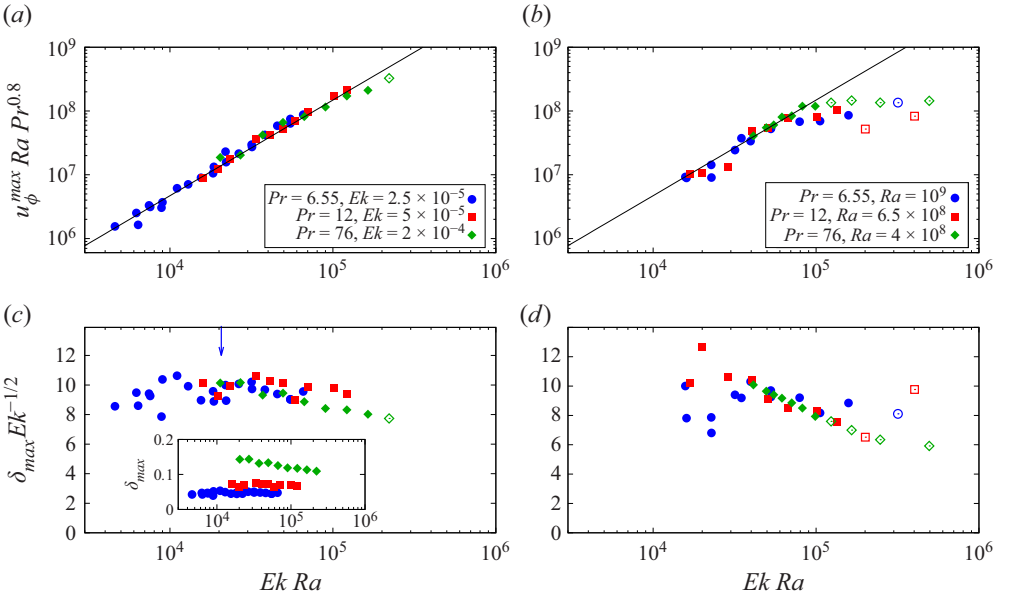

Figure 7. (*a*,*b*) Compensated maximal averaged azimuthal velocity $u_\phi^{max}\, Ra\, Pr^{0.8}$ as a function of $Ek\, Ra$. (*a*) Data acquired at constant Ek (datasets E1, E2, E3). (*b*) Data acquired at constant Ra (datasets R1, R2, R3). The solid black lines in (*a*) and (*b*) mark the same power law $\propto (Ek\, Ra)^{3/2}$. (*c*,*d*) Distance between the sidewall and the location of the azimuthal velocity maximum $\delta_{u_\phi^{max}}$. (*c*) Datasets E1, E2, E3 with constant Ek. (*d*) Datasets R1, R2, R3 taken at constant Ra. Open symbols in (*b*) and (*d*) mark data with $1/Ro < 1/Ro_t$ (see text). The inset in (*c*) shows the same data but plotted without the normalization $Ek^{-1/2}$. One sees that the data do not collapse on top of each other. The blue arrow in (*c*) marks the estimated location of the maximal heat transport for dataset E1.

data points ($Pr = 76$) seem to decrease slightly for larger $Ek\, Ra$, which might hint at the fact that buoyancy becomes too strong compared to Coriolis forces.

In figure 7(*d*), the same quantity is plotted but from data where Ra was constant (for a given Pr) and Ek was varied. We again plot with solid symbols data with $1/Ro \geq 1/Ro_t$, and use open symbols for data with $1/Ro < 1/Ro_t$. Clearly, the overlap of data with different Pr is rather good only for sufficiently large $1/Ro$ (solid symbols), and less good for the open symbols.

Data plotted as $\delta_{max}/\sqrt{Ek}$ (see figures 7*c*,*d*) collapse onto a single flat line, suggesting that $\delta_{max} \propto Ek^{1/2}$ and δ_{max} otherwise independent of Ra and Pr. We have already seen above (figure 5) that a similar scaling might also be visible in the data for δ_0, the thickness of the BZF. In fact, in figure 5(*b*), we have plotted already a purple line marking a power law $\delta_0 \propto Ek^{1/2}$. Now, for a better comparison, we plot in figure 8(*a*) both $\delta_{max}/\sqrt{Ek}$ and $\delta_0/\sqrt{Ek}$ as open and solid symbols inside the same graph. Clearly, the scatter of the data for δ_0 is much larger, but both follow straight lines over more than a decade in $Ek\, Ra$. However, in both cases, the green data ($Pr = 76$) for the largest $Ek\, Ra$ clearly decrease.

Figure 8(*b*) shows the ratio δ_0/δ_{max} as a function of $Ek\, Ra$. For this we have used all available data, and show data with constant Ek as open symbols, and data with constant Ra as solid symbols. The colour marks Pr. It becomes evident that the ratio $\delta_0/\delta_{max} \approx 2.6$ is a constant, therefore both δ_0 and δ_{max} should exhibit the same scaling relations with the

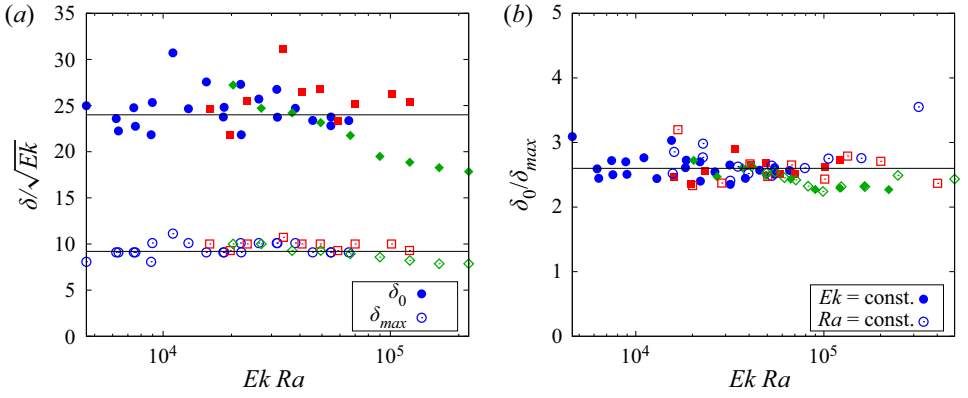

Figure 8. (*a*) Normalized length scales $\delta_0/\sqrt{Ek}$ (closed symbols) and $\delta_{max}/\sqrt{Ek}$ (open symbols) as functions of $Ek\,Ra$. Note that data are presented for datasets E1, E2 and E3, where in fact only Ra was varied. The straight black lines mark $\delta_0/\sqrt{Ek} = 24.0$ and $\delta_{max}/\sqrt{Ek} = 9.2$. (*b*) Ratio δ_0/δ_{max} as function of $Ek\,Ra$. Here, the open (closed) symbols are datasets with constant (varying) Ra and varying (constant) Ek. The different colours denote the different Prandtl numbers $Pr = 6.55$ (blue circles), 12 (red squares), 76 (green diamonds). The straight black line marks $\delta_0/\delta_{max} = 2.6$.

control parameters. However, we note that due to the rather large scattering of the data, small differences in the scaling exponents cannot be ruled out.

5. Conclusion

In this paper, we have presented measurements of the horizontal velocity at mid-height in a rotating Rayleigh–Bénard cell of aspect ratio $\Gamma = 1$ for various Ra, Ek and Pr using planar PIV. In these measurements, we could observe the boundary zonal flow (BZF) for the first time in an experiment, as a ring with positive average azimuthal velocity $\langle u_\phi \rangle > 0$ (cyclonic motion) surrounding a central region with $\langle u_\phi \rangle < 0$ (anticyclonic motion) as reported in Zhang *et al.* (2020, 2021*a*).

We studied the thickness of this zone (δ_0) as a function of Ek, Ra and Pr. Interpretation of the measured data is a somewhat difficult task, because on the one hand, the available parameter ranges cover no more than a decade, but also because we cover mainly small rotation rates, where the system is in the rotation-affected regime, where buoyancy is small compared to Coriolis forces. Hence it is unclear whether simple scaling laws are even expected in this regime and whether they will hold also in the rotation-dominated (geostrophic) regime. For example, for sufficiently large rotation rates (i.e. $1/Ro > 1/Ro_t$), δ_0 seems to follow $\propto 1/Ro^\alpha$, with $\alpha(Pr)$ being a function of Pr. While such a relation is possible (see e.g. Grossmann & Lohse 2000, 2001), finding the correct function $\alpha(Pr)$ is a difficult task for which many more data points over a much larger range need to be acquired to get reliable results.

Furthermore, we know that the rotation-affected regime as well as the rotation-dominated regime consists of smaller sub-regimes with transitions between them, as has been observed in measurements of the vertical heat flux (see e.g. Zhong & Ahlers 2010; Wei *et al.* 2015) and the flow configuration in the bulk (e.g. Stellmach *et al.* 2014; Plumley *et al.* 2016). In which way these regimes affect properties of the BZF is currently unclear. While it is somehow expected that transitions in the bulk from one regime to another also change how the BZF properties depend on Ra, Ek and Pr, it is also possible that

the BZF is decoupled from the dynamics in the bulk for sufficiently large rotation rates. As a result, scaling relations of its properties could hold in both the rotation-affected and rotation-dominated regimes. In this context, we want to remind the reader that data for $Pr = 6.55$ (datasets E1 and R1) cover not only parameter ranges, where a heat transport enhancement has been observed, but also ranges where a heat transport reduction is expected (see Zhong & Ahlers 2010; Weiss *et al.* 2016). In fact, the location of maximal heat transport enhancement for dataset E1 is marked with a blue arrow in figure 7(*c*). The trends of both u_ϕ^{max} and δ_{max} do not show significant differences at the left (*Nu* reduction) and the right (*Nu* enhancement) of this arrow.

Under the assumption of a simple power-law relationship of the form $\delta_0 \propto Ek^\alpha Ra^\beta Pr^\gamma$, our data suggest $\beta \approx 0$ or close by. In fact, only for the largest number, $Pr = 76$, do we find a slight decrease of δ_0 with increasing Ra, which might be due to insufficient rotation rates. This exponent is in contrast to $\beta = 1/4$, as found in numerical simulations by Zhang *et al.* (2021*a*). The exponent γ is around zero, or at least very small, which is in agreement with the scaling found in DNS, at least in the same Pr range (Zhang *et al.* 2021*a*). Regarding the Ek scaling, our data suggest $\alpha \approx 1/2$, again in contrast to DNS (Zhang *et al.* 2021*a*), where $\alpha = 2/3$ was suggested. A possible explanation for the difference between DNS and our experiment is the different parameter ranges. In fact, Zhang *et al.* (2021*a*) report results for $Pr > 1$ only for cylinders of aspect ratio $\Gamma = 1/2$. However, probably more important for the datasets of comparable Pr is that Ek in DNS is at least an order of magnitude smaller, and therefore Coriolis forces are much stronger compared to buoyancy in the simulation. It is indeed possible that the scaling relations that we find change for faster rotation and converge towards the findings in DNS.

In this respect, we note that in DNS, different scaling relations were found for δ_0 and δ_{max}, i.e. the distance from the sidewall at which the averaged azimuthal velocity is maximal. Here we find that both scale similarly $\propto Ek^{1/2}$. The maximal azimuthal velocity itself is found in our measurements to scale as $u_\phi^{max} \propto Ek^{3/2}\, Ra^{1/2}\, Pr^{-0.8}$. It is interesting that both δ_{max} and δ_0 are independent of Ra, but u_ϕ^{max} is not, suggesting that different mechanisms play a role here. In particular, the width is not just a result of a self-adjusting wall shear stress. Note in this respect that in this system, $Ek\,Ra$ represents the amount of thermal driving, compared to the minimal buoyancy that is necessary to initiate wall modes. On the other hand, δ_{max} and δ_0 are self-adjusting purely by Coriolis forces. To investigate this problem further, more measurements and simulations are necessary that indeed cover the entire range from the onset of wall modes up to the buoyancy-dominated regime.

Acknowledgements. We thank Olga Shishkina and Xuan Zhang for fruitful discussions. We also acknowledge support by Eberhard Bodenschatz for providing technical and administrative infrastructure for this project.

Funding. We acknowledge financial support by the Deutsche Forschungsgemeinschaft (DFG) through grant WE 5011/4-1, and from the European High-Performance Infrastructure in Turbulence programme (EuHIT). D.F. received a travel grant from the Deutscher Akademischer Austauschdienst (DAAD).

Declaration of interests. The authors report no conflict of interests.

Author ORCIDs.
Stephan Weiss https://orcid.org/0000-0003-1626-3780.

References

Ahlers, G., *et al.* 2022 Aspect ratio dependence of heat transfer in a cylindrical Rayleigh–Bénard cell. *Phys. Rev. Lett.* **128**, 084501.

Ahlers, G., Grossmann, S. & Lohse, D. 2009 Heat transfer and large scale dynamics in turbulent Rayleigh–Bénard convection. *Rev. Mod. Phys.* **81** (2), 503–538.

Brown, E., Funfschilling, D. & Ahlers, G. 2007 Anomalous Reynolds-number scaling in turbulent Rayleigh–Bénard convection. *J. Stat. Mech.* **2007**, P10005.

Buell, J.C. & Catton, I. 1983 Effects of rotation on the stability of a bounded cylindrical layer of fluid heated from below. *Phys. Fluids* **26**, 892–896.

Chandrasekhar, S. 1961 *Hydrodynamic and Hydromagnetic Stability*. Dover.

Chelton, D.B & Schlax, M.G 1996 Global observations of oceanic Rossby waves. *Science* **272** (5259), 234–238.

Ciliberto, S., Cioni, S. & Laroche, C. 1996 Large-scale flow properties of turbulent thermal convection. *Phys. Rev.* E **54**, R5901–R5904.

Ecke, R.E., Zhong, F. & Knobloch, E. 1992 Hopf bifurcation with broken reflection symmetry in rotating Rayleigh–Bénard convection. *Europhys. Lett.* **19**, 177–182.

Favier, B. & Knobloch, E. 2020 Robust wall states in rapidly rotating Rayleigh–Bénard convection. *J. Fluid Mech.* **895**, R1.

Goldstein, H.F., Knobloch, E., Mercader, I. & Net, M. 1993 Convection in a rotating cylinder. Part 1. Linear theory for moderate Prandtl numbers. *J. Fluid Mech.* **248**, 583–604.

Grossmann, S. & Lohse, D. 2000 Scaling in thermal convection: a unifying view. *J. Fluid. Mech.* **407**, 27–56.

Grossmann, S. & Lohse, D. 2001 Thermal convection for large Prandtl number. *Phys. Rev. Lett.* **86**, 3316–3319.

Grossmann, S. & Lohse, D 2002 Prandtl and Rayleigh number dependence of the Reynolds number in turbulent thermal convection. *Phys. Rev.* E **66**, 016305.

He, X., Funfschilling, D., Bodenschatz, E. & Ahlers, G. 2012 Heat transport by turbulent Rayleigh–Bénard convection for $Pr \approx 0.8$ and $4 \times 10^{11} < Ra < 2 \times 10^{14}$: ultimate-state transition for aspect ratio $\gamma = 1.00$. *New. J. Phys.* **14**, 063030.

Heimpel, M., Aurnou, J. & Wicht, J. 2005 Simulation of equatorial and high-latitude jets on Jupiter in a deep convection model. *Nature* **438**, 193–196.

Herrmann, J. & Busse, F.H. 1993 Asymptotic theory of wall-attached convection in a rotating fluid layer. *J. Fluid Mech.* **255**, 183–194.

Horn, S. & Shishkina, O. 2015 Toroidal and poloidal energy in rotating Rayleigh–Bénard convection. *J. Fluid Mech.* **762**, 232–255.

Julien, K., Legg, S., Mcwilliams, J. & Werne, J. 1996 Rapidly rotating turbulent Rayleigh–Bénard convection. *J. Fluid Mech.* **322**, 243–273.

Krishnamurti, R. & Howard, L.N. 1981 Large scale flow generation in turbulent convection. *Proc. Natl Acad. Sci.* **78**, 1981–1985.

Kunnen, R.P.J. 2020 The geostrophic regime of rapidly rotating turbulent convection. *J. Turbul.* **22**, 267–296.

Kunnen, R.P.J., Clercx, H.J.H. & Geurts, B.J. 2006 Heat flux intensification by vortical flow localization in rotating convection. *Phys. Rev.* E **74**, 056306.

Kunnen, R.P.J., Stevens, R.J.A.M., Overkamp, J., Sun, C., van Heijst, G.J.F. & Clercx, H.J.H. 2011 The role of Stewartson and Ekman layers in turbulent rotating Rayleigh–Bénard convection. *J. Fluid Mech.* **688**, 422–442.

Kuo, E.Y. & Cross, M.C. 1993 Traveling-wave wall states in rotating Rayleigh–Bénard convection. *Phys. Rev.* E **47**, R2245–R2248.

Liu, Y. & Ecke, R.E. 1997 Heat transport scaling in turbulent Rayleigh–Bénard convection: effects of rotation and Prandtl number. *Phys. Rev. Lett.* **79**, 2257–2260.

Malkus, W.V.R. 1954 The heat transport and spectrum of thermal turbulence. *Proc. R. Soc. Lond.* A **225** (1161), 196–212.

Plumley, M., Julien, K., Marti, P. & Stellmach, S. 2016 The effects of Ekman pumping on quasi-geostrophic Rayleigh–Bénard convection. *J. Fluid Mech.* **803**, 51–71.

Proudman, J. 1916 On the motion of solids in a liquid possessing vorticity. *Proc. R. Soc. Lond.* A **92** (642), 408–424.

Reuter, D.C., *et al.* 2007 Jupiter cloud composition, stratification, convection, and wave motion: a view from new horizons. *Science* **318** (5848), 223–225.

Rossby, H.T. 1969 A study of Bénard convection with and without rotation. *J. Fluid Mech.* **36**, 309–335.

SANO, M., WU, X.Z. & LIBCHABER, A. 1989 Turbulence in helium-gas free convection. *Phys. Rev.* A **40**, 6421–6430.

SHISHKINA, O. 2020 Tenacious wall states in thermal convection in rapidly rotating containers. *J. Fluid Mech.* **898**, F1.

STELLMACH, S., LISCHPER, M., JULIEN, K., VASIL, G., CHENG, J.S., RIBEIRO, A., KING, E.M. & AURNOU, J.M. 2014 Approaching the asymptotic regime of rapidly rotating convection: boundary layers versus interior dynamics. *Phys. Rev. Lett.* **113**, 254501.

STEWARTSON, K. 1957 On almost rigid rotations. *J. Fluid Mech.* **3**, 17–26.

STEWARTSON, K. 1966 On almost rigid rotations. Part 2. *J. Fluid Mech.* **26** (1), 131–144.

SUN, C. & XIA, K.-Q. 2005 Scaling of the Reynolds number in turbulent thermal convection. *Phys. Rev.* E **72**, 067302.

TAYLOR, G.I. 1921 Experiments with rotating fluids. *Proc. R. Soc. Lond.* A **100**, 114–121.

WANG, C.-S. 2018 ParaPIV. https://www.researchgate.net/publication/327392231_ParaPIV.

WEDI, M., VAN GILS, D.P.M., BODENSCHATZ, E. & WEISS, S. 2021 Rotating turbulent thermal convection at very large Rayleigh numbers. *J. Fluid Mech.* **912**, A30.

WEI, P., WEISS, S. & AHLERS, G. 2015 Multiple transitions in rotating turbulent Rayleigh–Bénard convection. *Phys. Rev. Lett.* **114**, 114506.

WEISS, S. & AHLERS, G. 2011*a* Heat transport by turbulent rotating Rayleigh–Bénard convection and its dependence on the aspect ratio. *J. Fluid Mech.* **684**, 407–426.

WEISS, S. & AHLERS, G. 2011*b* The large-scale flow structure in turbulent rotating Rayleigh–Bénard convection. *J. Fluid Mech.* **688**, 461–492.

WEISS, S., WEI, P. & AHLERS, G. 2016 Heat-transport enhancement in rotating turbulent Rayleigh–Bénard convection. *Phys. Rev.* E **93**, 043102.

DE WIT, X.M., GUZMÁN, A.J.A., MADONIA, M., CHENG, J.S., CLERCX, H.J.H. & KUNNEN, R.P.J. 2020 Turbulent rotating convection confined in a slender cylinder: the sidewall circulation. *Phys. Rev. Fluids* **5**, 023502.

ZHANG, K. & LIAO, X. 2009 The onset of convection in rotating circular cylinders with experimental boundary conditions. *J. Fluid Mech.* **622**, 63–73.

ZHANG, K. & SCHUBERT, G. 1996 Penetrative convection and zonal flow on Jupiter. *Science* **273** (5277), 941–943.

ZHANG, X., ECKE, R.E. & SHISHKINA, O. 2021*a* Boundary zonal flows in rapidly rotating turbulent thermal convection. *J. Fluid Mech.* **915**, A62.

ZHANG, X., ECKE, R.E. & SHISHKINA, O. 2021*b* Boundary zonal flows in rapidly rotating turbulent thermal convection. *J. Fluid Mech.* **915**, A62.

ZHANG, X., VAN GILS, D.P.M., HORN, S., WEDI, M., ZWIRNER, L., AHLERS, G., ECKE, R.E., WEISS, S., BODENSCHATZ, E. & SHISHKINA, O. 2020 Boundary zonal flow in rotating turbulent Rayleigh-Bénard convection. *Phys. Rev. Lett.* **124**, 084505.

ZHONG, F., ECKE, R. & STEINBERG, V. 1991 Asymmetric modes and the transition to vortex structures in rotating Rayleigh–Bénard convection. *Phys. Rev. Lett.* **67**, 2473–2476.

ZHONG, F., ECKE, R. & STEINBERG, V. 1993 Rotating Rayleigh–Bénard convection: asymmetric modes and vortex states. *J. Fluid Mech.* **249**, 135–159.

ZHONG, J.-Q. & AHLERS, G. 2010 Heat transport and the large-scale circulation in rotating turbulent Rayleigh–Bénard convection. *J. Fluid Mech.* **665**, 300–333.

ZHONG, J.-Q., STEVENS, R.J.A.M., CLERCX, H.J.H., VERZICCO, R., LOHSE, D. & AHLERS, G. 2009 Prandtl-, Rayleigh-, and Rossby-number dependence of heat transport in turbulent rotating Rayleigh–Bénard convection. *Phys. Rev. Lett.* **102**, 044502.

ZWIRNER, L., EMRAN, M.S., SCHINDLER, F., SINGH, S., ECKERT, S., VOGT, T. & SHISHKINA, O. 2021 Dynamics and length scales in vertical convection of liquid metals. *J. Fluid Mech.* **932**, A9.